



ELSEVIER

Contents lists available at ScienceDirect

Planetary and Space Science

journal homepage: www.elsevier.com/locate/pss

Raman imaging of extraterrestrial materials

Alian Wang^{a,*}, Randy L. Korotev^a, Bradley L. Jolliff^a, Zongcheng Ling^b^a Department of Earth and Planetary Sciences and McDonnell Center for the Space Sciences, Washington University in St. Louis, MO, USA^b School of Space Science and Physics, Shandong University, Weihai Campus, China

ARTICLE INFO

Article history:

Received 27 May 2014

Received in revised form

19 September 2014

Accepted 8 October 2014

Available online 18 October 2014

Keywords:

Laser Raman spectroscopy

Molecular phase identification

Spatial distribution

Extraterrestrial material analysis

ABSTRACT

Laser Raman Spectroscopy has been proposed and is under extensive development for surface exploration missions to planetary bodies of our Solar System. It reveals information on molecular structure and chemistry. The spatial distribution of molecular species in natural geological samples and planetary materials has significance for the geological processes by which they formed. Raman imaging is the best way to combine the molecular identification and characterization of geologic materials with their spatial distribution. This paper reports Raman imaging studies of five types of extraterrestrial materials and three terrestrial samples using a state-of-the-art Raman imaging system. The Raman spectral features of major, minor, and trace species in these samples, together with their spatial correlations revealed by these Raman imaging studies indicate the genetic relationships and the geological processes that these materials have been experienced. For robotic planetary surface exploration mission, a simple yet very useful molecular map of a sample can be generated by using line-scan or grid-scan of an in situ Raman system with tightly focused laser beam.

© 2014 Elsevier Ltd. All rights reserved.

1. Introduction

Laser Raman Spectroscopy has been proposed and is under extensive development for surface exploration missions to planetary bodies of the Solar System (Wang et al., 1995, 1998, 2003; Wang and Lambert, 2013; Rull and Martinez-Frias, 2006). A laser Raman spectrum presents the inelastically scattered light photons from a sample when irradiated with an excitation laser line of wavelength λ_0 . The wavelength shifts of the spectral peaks in a Raman spectrum relative to the excitation laser wavelength ($\Delta\lambda = \lambda_{\text{meas}} \pm \lambda_0$, expressed in cm^{-1}) reveal the energies of vibrational modes of chemical bonds (or molecular species) in the sample. A Raman spectrum can be excited by laser lines in IR, VIS, and UV spectral ranges, because it observes the wavelength differences. Thus ordinary Raman spectrometers would allow information about molecular structure and chemistry, whose energies of transitions are in the mid-IR spectral range, to be observed in the visible spectral range. This instrumentation concept allows the usage of highly matured opto-electronics developed for the visible spectral range to be used in flight Raman system development.

In normal cases, Raman measurement is non-destructive because the laser does not vaporize the materials, but caution should be taken for heat-sensitive samples. Raman measurement gets information on the *as is* status of organic and inorganic molecular species in solids (crystalline and amorphous), liquids, and gases. The laser Raman measurements can be non-invasive because the laser beam and Raman scattered photons can penetrate through optically transparent materials, such as laboratory reaction vials, through a window on the process line of an in-situ resource utilization (ISRU) platform on a planetary surface (e.g., Moon or Mars), or through a window on a descending vessel to a planetary surface (e.g., Venus).

During the robotic investigation of a rock on a planetary surface (e.g., Mars) or laboratory study of a sample with an extraterrestrial origin, it is desirable to obtain both information on the molecular species and the spatial distribution of the species in the sample. Raman imaging is the best way to realize this combined analysis. A Raman imaging system generates a molecular map on the basis of characteristic Raman spectral features of molecular species in the analyzed sample. The method of generating a Raman image can be very simple and straightforward for robotic exploration (e.g., line-scan or grid scan, Haskin et al., 1997), or can be more sophisticated and detailed in the laboratory (Nasdala et al., 2012). This paper reports results of a set of Raman imaging studies of extraterrestrial materials using a state-of-the-art Raman imaging system. Five types of extraterrestrial materials were selected for this preliminary Raman imaging investigation: Apollo samples from the Moon, lunar meteorites, martian meteorites, achondrites, and carbonaceous chondrites.

* Correspondence to: Room 338, Rudolph Hall, Department of Earth and Planetary Sciences, Washington University in St. Louis, 63130 MO, USA.
Tel.: +314 935 5851; fax: +314 935 7361.

E-mail address: alianw@levee.wustl.edu (A. Wang).

2. Raman imaging and its application to extraterrestrial materials

In a Raman imaging measurement, we obtain a Raman data “cube” from each sampling spot on a 2 dimensional sample surface with the 3rd dimension of data cube being the Raman spectrum. Recently on transparent (relative to laser wavelength used) or semi-transparent sample, 4D Raman image data cube can be obtained with one Raman spectrum from each sampling spot in a 3D volume of the analyzed sample. Using this data cube, one can generate multiple Raman images that reflect the spatial distribution of molecular species, as well as the spatial distribution of a specific property of a molecular species, in the analyzed sample. For example, one can (1) use the major Raman peak positions and spectral patterns of the minerals olivine, pyroxene, plagioclase, ilmenite, and other trace phases to generate a map, i.e., spatial distribution of all minerals in lunar rocks; (2) use the Raman peak intensity (or peak area) to generate the abundance distribution and the map of the degree of structural ordering of reduced carbon in martian meteorites (Steele et al., 2007, 2010, 2012a, 2012b) or carbonaceous chondrites (Fries and Steele, 2008); (3) use the shift of a Raman peak central position to generate a map of chemical zoning [e.g., $Mg/(Mg+Fe+Ca)$] in a pyroxene grain of a lunar or martian meteorite (Seddio et al., 2015); and (4) use the change in Raman peak position or the change in peak width to generate a map of structural distortion, crystallinity variation, or mechanical stress in an Si sample (Gogots et al., 1999). In these maps, spatial correlations of the different phases and the compositional and structural variations in a single phase can reveal evidence of past physical, chemical, and biological processes, and thus demonstrate potential genetic relationships.

Extraterrestrial samples are keys to understanding the properties of other objects (planets, satellites, asteroids, comets) in the Solar System and of the building blocks during different periods of Solar System formation and stellar evolution. Characterizations of the atomic, isotopic, and molecular species in such samples are essential. Examples of some of the processes affecting extraterrestrial samples that may differ from processes on Earth include the impact and space weathering of surface materials on airless bodies like the Moon and asteroids; the physical and chemical weathering of surface and subsurface materials on Mars and Venus under very different atmospheric and environmental conditions; the cryogenic tectonic processes on icy satellites (e.g., Europa and Titan) in a high radiation environment; the violent degassing and loss of surface layers of a comet when approaching the Sun; and the wide range of metamorphism with temperature and chemical changes (sometimes involving hydrous and organic species) during the formation of meteorites; and the atomic/isotopic differentiation and molecular formation in IDPs within the early solar nebula. These processes, and the physical and chemical conditions that stimulated and sustained these processes, are all crucial for understanding how the Solar System and life began and evolved. Together with atomic and isotopic imaging, molecular imaging generated by Raman imaging studies of extraterrestrial samples can help to answer these questions.

2.1. Various Raman imaging methodologies

Different methodologies exist to collect a Raman imaging data cube; these can be classified in two basic approaches. One approach uses a spatially broad (normally defocused) excitation laser beam to stimulate a large area in a sample, and then to have the Raman photons from all sampling spots in that area pass simultaneously through a series of wavelength windows, thus forming a full-range Raman spectrum at each spot. Filter technologies are used in this type of Raman imaging in which the Raman photons of selected wavelength are allowed to reach the detector by tuning the band

pass of a single filter or multiple filters, such as an Acoustic Optical Tunable Filter (AOTF) or wheel-filter(s) with adjustable incidence angle. An alternative method in this approach is a non-filter technology that also benefits from a broad excitation beam. It uses a Raman probe made of an optical fiber bundle that contains hundreds to thousands of individual optical fibers to collect Raman photons and to use a conventional spectrograph to generate a Raman spectrum for each fiber. The positional information of all spots in an analyzed sample is stored in the position of each optical fiber in the fiber bundle. The advantage of this Raman imaging approach is fast image acquisition. The disadvantage is the low Raman signal strength (because the laser beam is defocused) and the potentially significant interference from fluorescence in some samples. This approach is suitable for imaging materials with large Raman-scattering cross sections but with little or no fluorescence, such as synthetic pharmaceutical samples.

Most natural geological materials are medium to weak Raman scatterers and fluorescence interferences occur in many terrestrial geological materials. Therefore, the more efficient Raman imaging methodology for geological samples is to use the second approach. It uses a tightly focused excitation laser beam to generate a Raman spectrum with good S/N at a single spot in the sample, then to use a scanning mechanism to move to another sample spot and sequentially build a Raman image data cube. In other words, the first Raman imaging approach scans in wavelength space and the second Raman imaging approach scans in X-Y-Z space.

For the second Raman imaging approach, a variety of X-Y-Z spatial scan technologies has been developed, as follows. (1) A highly accurate translational microscopic stage can be used to sequentially position the spots of a sample (along a line or a 2D & 3D grid) under a tightly focused laser beam. (2) A 2-D galvanometric motor can be used to scan a tightly focused laser beam onto the spots of a small sampling area (a few tens of micrometers) covered by the field of view (FOV) of a microscopic objective used for the Raman measurement, and then moving in the X-Y directions of a microscopic stage to enlarge the imaged area (mm to cm). (3) A slightly defocused laser beam can be used to irradiate an elliptically shaped area on the analyzed sample and then the Raman spectra can be collected from all spots in this elliptical area simultaneously. The microscopic stage can then be moved in the direction perpendicular to the long axis of the ellipse and to collect the Raman data cube of a large area. (4) A combination of laser optics, high accuracy stage motion, and synchronized CCD readout can be used for fast Raman imaging of a large sampling area (details in following paragraph). The advantage of the second Raman imaging approach is a generally high Raman signal strength. The disadvantage is longer acquisition time for an image than the first approach, especially when using a grid scan [i.e., (1) above]. However, this disadvantage has been greatly reduced by new designs of state-of-the-art Raman imaging systems, which can perform type (2), (3), and (4) scans in mm to cm distance scales (depending on spatial resolution) in hours on geological samples.

2.2. Raman imaging system used for this study

We built a new Raman imaging laboratory at Washington University in St. Louis and installed an inVia[®] Raman System (Renishaw Company) in December 2011. The system consists of a spectrometer capable of collecting Raman spectra stimulated by five excitation laser lines. The system is also an imager using methodologies (1), (3), and (4) described above to make high quality Raman images. When using methodology (1) in a high-spatial-resolution mode, the laser beam is focused to reach the diffraction limit ($< 1 \mu\text{m}$ using a 50x objective for 532 nm line); the stepping motor of the microscopic stage has $\sim 100 \text{ nm}$ accuracy and precision. The combination of these two aspects can produce an “over-sampling” in Raman signal collection that

can generate a Raman image data cube with spatial resolution of $\sim 250\text{--}300$ nm in the X-Y plane and ~ 500 nm in the Z direction, variable at different excitation laser wavelengths.

An imaging methodology [(4) above] of the inVia system is called StreamLine™; this method achieves both high spatial resolution (μm) Raman imaging and short data acquisitions from geological samples. This imaging mode combines three functions at the same time. First, an elliptical-shaped laser beam spot is used and Raman photons from all sampled points in this ellipse are sent to an area on the CCD camera. In that area, each column of CCD pixels corresponds to all spots irradiated by the elliptical laser spot, and each row of CCD pixels records a Raman spectrum from one of the sampling spots. Second, the microscopic stage moves *along the long-axis of the ellipse*, thus each spot within the ellipse on the sample is repeatedly irradiated by the laser beam during the scan. Third, during the whole period of this stage-scan, the data readout of the CCD camera is synchronized, i.e., it continuously reads out the data from each row of pixels during stage movement. The spectral data from a single spot within the sampling ellipse is collected (e.g., 10–30 times) and co-added based on the synchronization of stage motion and the CCD readout, which improves the S/N in the Raman spectrum from each spot. The width of the elliptical laser beam and the step size of stage motion determine the spatial resolution of the Streamline™ Raman imaging (can be μm to sub- μm). The continuous CCD readout shortens data acquisition (i.e., shutter open-close only once in an imaging measurement), thus the StreamLine™ imaging data cube collection is extremely fast. Many high quality Raman imaging data cubes (with 1.3 μm spatial resolution) presented in this manuscript were collected in less than one hour.

Because laser Raman spectroscopy can be stimulated by various wavelengths, such as IR, VIS, and UV, our inVia Raman imaging system has five laser wavelengths: 785 nm line of a, diode laser; 632.8 nm line of a, He-Ne laser; 532 nm line of a, diode-pumped solid-state laser, and 442 nm line and 325 nm line of a He-Cd laser. A Raman system with multiple excitation laser wavelengths facilitates the study of a wide variety of materials because Raman cross sections of materials change with excitation wavelength. Some laser wavelengths enhance Raman signals by inducing Raman resonance effects

(Marshall et al., 2007). Some laser wavelengths help to avoid the interference of fluorescence generated by specific species in terrestrial samples. Up to now, the green laser excitation (e.g., 532 nm) has been demonstrated to be the most efficient one for the characterization of general mineralogy and biomarkers such as carotenoids (Marshall et al., 2010; Marshall and Wang, 2010), whereas UV (< 400 nm) and IR (785 nm) laser excitations have been suggested to have advantages for the detection of DNA, RNA, and proteins (Edwards et al., 2005a, 2005b, 2007; Villar et al., 2005, 2006).

Rock chips with flat-cut surfaces, thin sections of geological samples and sections of biological samples, mineral powders or soils, liquid samples in capillaries, reaction vials or petri dishes made of fused silica glass, as well as liquid and gaseous species in fluid inclusions of rock samples (see below) can all be analyzed using this new Raman imaging system.

3. Demonstration of Raman imaging capability on terrestrial samples

We first use three terrestrial samples to demonstrate the capability of state-of-the-art Raman imaging.

3.1. Raman imaging of a species in three dimensional space – CH_4 inclusions in quartz matrix

A quartz crystal with thousands of fluid inclusions was studied. The size of fluid inclusions varies from < 1 to 300 μm , with a highly heterogeneous distribution in the quartz matrix (Fig. 1a). A white-light image shows that the fluid inclusions occur along fractures (not shown in Fig. 1a) in X-Y-Z space of the quartz matrix. For example, many of the small fluid inclusions occur in groups that have a planar distribution. The fluid phase in all these inclusions is gaseous methane. Fig. 1b shows the Raman peak of CH_4 collected from one of these fluid inclusions. The Raman peak position of CH_4 occurs at 2914 cm^{-1} .

The collection of Raman signals in the X-Y plane was made by a grid scan of the microscopic stage, thus a tightly focused laser spot (wavelength $\lambda=532$ nm) would interrogate sequentially the spots on a pre-selected grid at the focus plane of the laser beam (at the

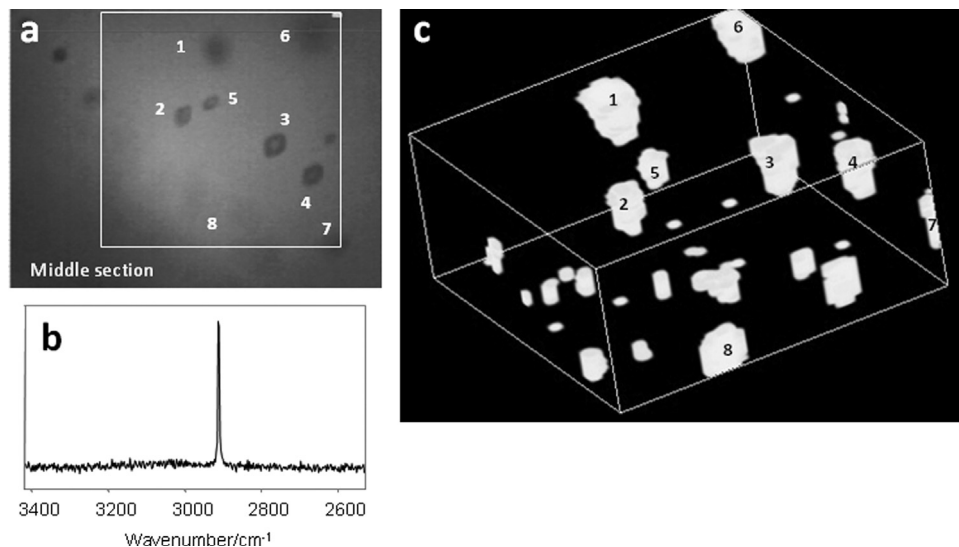


Fig. 1. Three-dimensional Raman imaging of CH_4 fluid inclusions in a quartz matrix.

a. B/W image of fluid inclusions in a zone at middle Z depth of a quartz rock chip.

b. Typical Raman spectra of CH_4 from inclusion and Qtz matrix.

c. Spatial distribution of CH_4 fluid inclusions in this zone – Raman imaging data cube collection using 532 nm excitation laser line, 50x long-working distance microscopic objective, 3D volume imaging mode with $2 \times 2 \times 2$ μm steps, that correspond 2208 spots analysis per layer for 50 layers that covers a $100 \times 110 \times 100$ μm volume in quartz matrix. The colors represent the CH_4 Raman peak intensity at each spot (White=higher intensity, gray=lower intensity) (please see on-line version for color images) (please see on-line version for color images).

surface of quartz, or beneath), in a $100\ \mu\text{m} \times 110\ \mu\text{m}$ area (2208 spots per layer, $2 \times 2\ \mu\text{m}$ grid). Collection of Raman signals in the Z dimension was made by moving the microscopic stage at $2\ \mu\text{m}$ steps through a $100\ \mu\text{m}$ distance (a total of 50 layers), thus the inclusions at different depths in the quartz matrix were intersected with a laser beam focused at that depth. The Raman image generated from the Raman peak position and peak intensity of CH_4 gas correctly represents the spatial distribution of these CH_4 fluid inclusions in the quartz matrix, including their sizes and their spatial relationships (Fig. 1c, in comparison with Fig. 1a, a photo of the mid-section of the analyzed volume). Currently, the high-confocal mode cannot be used in collecting the Raman signals through the volume, which affects the shape of fluid inclusions in the Raman image, but this effect is correctable by software.

The Raman image in Fig. 1c was built on the basis of the CH_4 Raman spectrum, by first using a curve-fitting procedure to generate a smooth Raman peak pattern of CH_4 from a raw spectrum. This smooth pattern was then used as the component spectrum in a Direct Classical Least Squares Component Analysis (DCLS) map-building procedure that searched through all 110,400 spectra in the collected Raman image data cube and built up the molecular image of CH_4 -bearing inclusions in the SiO_2 matrix.

3.2. Raman imaging of a property – crystallinity of reduced carbon in a chert

Among carbon-bearing phases, reduced carbon is of special interest in planetary sciences because it might be the only remaining evidence of ancient life forms on Mars. The harsh environmental conditions (i.e., extremely dry, low temperature, large temperature swing cycles, high levels of UV light and galactic cosmic ray, and frequent dust storms) in the Amazonian period (Pavlov et al., 2012) may have destroyed the molecular forms of biomarkers at most locations at surface and shallow subsurface, with only reduced carbon remaining. We need to know how well reduced carbon can be detected and characterized (structural ordering reflects the thermal environment) within geological context.

For this study, we used a carbonaceous chert from the Onverwacht subdivision, Swaziland supergroup, Barberton greenstone belt, South Africa (Walsh and Lowe, 1985; Walsh, 1992). Three types of carbonaceous chert occur there: black-and-white banded chert, massive black chert, and laminated black chert. Thin section MW9-6 was used for this Raman imaging study. Previous Raman studies on the same sample were done using a microbeam Raman spectrometer ($\sim 6\ \mu\text{m}$ laser beam diameter) and demonstrated a 50 ppm detection sensitivity for carbonaceous materials in this chert (Wang et al., 2001).

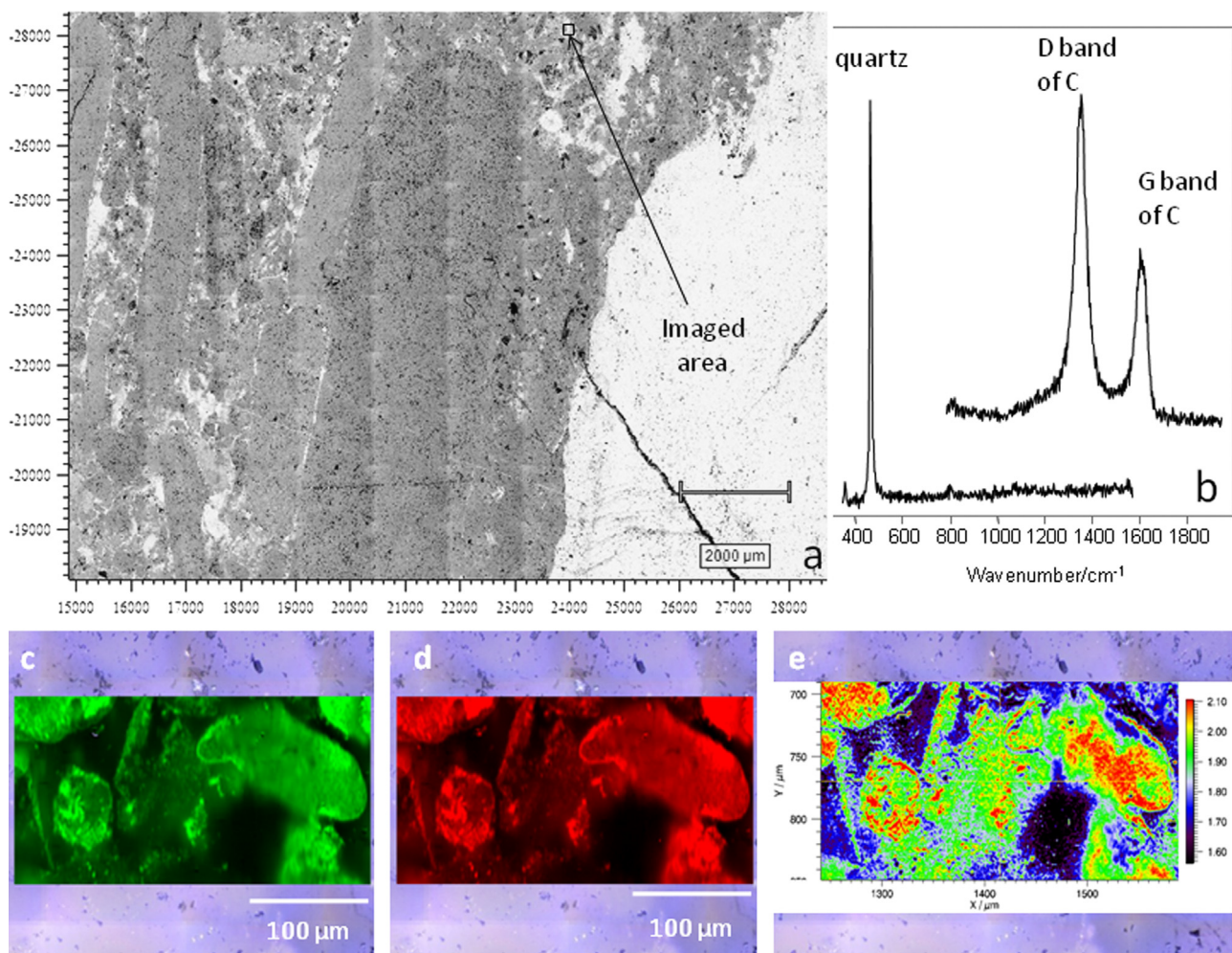


Fig. 2. Raman imaging showing the distribution of carbon crystallinity in a South African (SA) chert. a. B/W image of thin section of SA chert. A red rectangle marks the area for Raman imaging study. b. Typical Raman spectra from this sample: quartz and carbonaceous material. c. Raman image generated from peak area of G band – the abundance is expressed by brightness of the green color. d. Raman image generated from peak area of D band – the abundance is expressed by brightness of the red color. e. Raman image generated from the peak area ratios of G to D band – the differences in crystallinity of these carbonaceous materials are shown in rainbow colors.

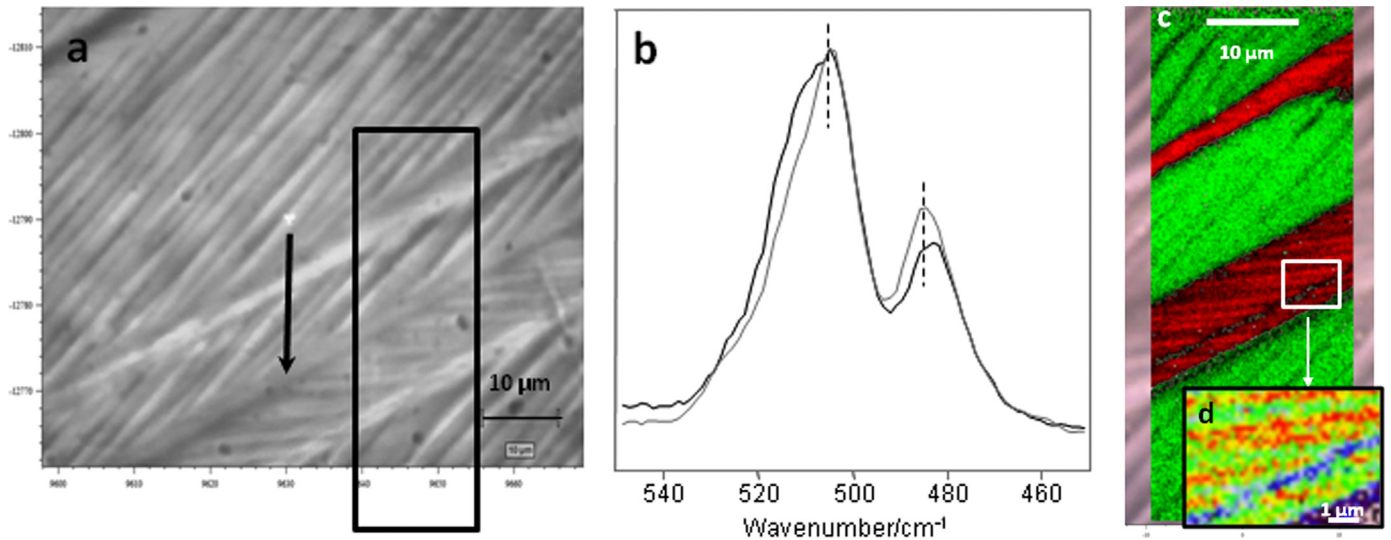


Fig. 3. Raman imaging with sub-micrometer spatial resolution of Huttenlocher intergrowths in a plagioclase grain.

- Optical image of an area of Huttenlocher intergrowths in a feldspar grain in thin section OGG-145 thin section, Nordland anorthosite from SW Greenland, where Raman spot analyses were made (marked by a dark arrow) and the Streamline™ High-Resolution Raman imaging data cube (marked by dark rectangle) was collected.
- Typical Raman spectra from two sets of lamellae, which show the spectral feature differences representing zoned mineral chemistry (An70–82) and structure.
- Raman image of the two sets of Huttenlocher intergrowth lamellae in OGG-145 based on their difference in Raman spectral features. The red and green colors distinguish the lamellae with different Raman spectral features, the shades of red (or green) represent the Raman signal intensity of one of the two different plagioclase compositions.
- Details in the Raman image (circled by a white rectangle in Fig. 3c) in which the different reddish shades were replaced by rainbow colors to emphasize the differences in Raman spectra and Raman signal strength. The size of features (red, green, and blue colored) demonstrate that sub-micrometer spatial resolution is obtained from this measurement.

Fig. 2a shows the white-light image of thin section MW9-6 and Fig. 2b shows typical Raman spectra of the quartz matrix and the reduced carbon in this chert sample. The strong Raman peak (G band) near 1595 cm^{-1} is from the first order E_{2g2} fundamental vibration of graphite. Another major peak near 1350 cm^{-1} (D band) and in some cases a shoulder $\sim 1620\text{ cm}^{-1}$ are induced by structural disorder in the carbonaceous material. The relative intensities of G and D bands vary according to the level of structural distortion, i.e., the crystallinity of carbonaceous materials. Previous Raman studies (Nemanich and Solin, 1979; Wang et al., 1989; Pasteris and Wopenka, 1991; Wopenka and Pasteris, 1993) have established a quantitative correlation between the ratio of the peak area of G and D bands and in-plane crystallite size L_a in the structure of carbonaceous materials. Some studies have related this ratio and other Raman parameters to the metamorphic grade of the rock in which the carbonaceous materials reside (Pasteris and Wopenka, 1991).

A Raman image cube was collected in a darker area in thin section MW9-6 (marked by a black square in Fig. 2a), using the 532 nm laser line, 50x objective, Streamline™ imaging mode, with 33,087 data points (269×123) collected at $1.3\text{ }\mu\text{m}$ per step. In order to generate a map of the variation in crystallinity of carbonaceous materials, we first used the spectral curve fitting procedure to get the smooth Raman peak patterns of the G and D bands. These two spectral patterns were then used as component spectra in a DCLS mapping procedure that searched through all 33,087 spectra in the collected Raman image cube and generated two images: one based on the peak area of the G band (Fig. 2c) and one based on the peak area of the D band (Fig. 2d), in which the intensity of colors (red or green) correspond to the peak area values, i.e., the abundance of carbonaceous materials. By ratio of these two images, the spatial distribution of a derived property (Fig. 2e), i.e., the variation in crystallinity of carbonaceous materials in the studied area, was generated. The central portion of the mapped carbonaceous grains appears to have a slightly higher structural order than the rims. The heterogeneity in the structural ordering of carbonaceous materials in this chert

sample can be linked to the conditions during its formation and the subsequent metamorphic process that it experienced.

3.3. Sub-micrometer Raman imaging – Huttenlocher intergrowths in plagioclase

To demonstrate that sub-micrometer spatial resolution can actually be achieved by the inVia Raman imager, we collected a Raman image cube from an area of intergrowths of two chemically distinct types of feldspar with extremely tight spatial occurrence. A thin section of Nordland anorthosite from SW Greenland, OGG-145, contains plagioclase with Huttenlocher intergrowths (Fig. 3a). The intergrowth appears as two sets of lamellae (thickness of individual lamellae is $\sim 1\text{--}2\text{ }\mu\text{m}$) with different spatial orientations. The separation of lamellae is caused by a slightly different Ca/(Ca+Na) ratio (different An content) in the feldspar that corresponds also a structural change related to a coupled substitution of Al and Si in tetrahedral sites. The Huttenlocher intergrowths would normally appear in the An range of 65–85 in slowly cooled rocks. In this sample, the An range is 70–82 (Dymek and Owens, 2001).

Fig. 3b shows two typical Raman spectra taken from individual spots along a line crossing the Huttenlocher intergrowth lamellae (indicated by a black arrow in Fig. 3a). Feldspar of various compositions have major Raman peaks in the $540\text{--}460\text{ cm}^{-1}$ spectral range (Freeman et al., 2008). In this sample, the major Raman peak near 510 cm^{-1} consists of two component peaks. Between the two typical Raman spectra throughout the Huttenlocher lamellae (Fig. 3b), the changes are the relative intensities of these two component peaks and the central position of the second Raman peak near 485 cm^{-1} . Based on these two spectral features that distinguish the sets of intergrowth lamellae, we generated a Raman image of the Huttenlocher intergrowth (Fig. 3c) in which red and green colors distinguish lamellae with different Raman spectral features wherein the shades of red (or green) (Fig. 3c) represent the Raman signal strength. Fig. 3d shows details of a red-colored area in Fig. 3c, circled by a white rectangle, in which

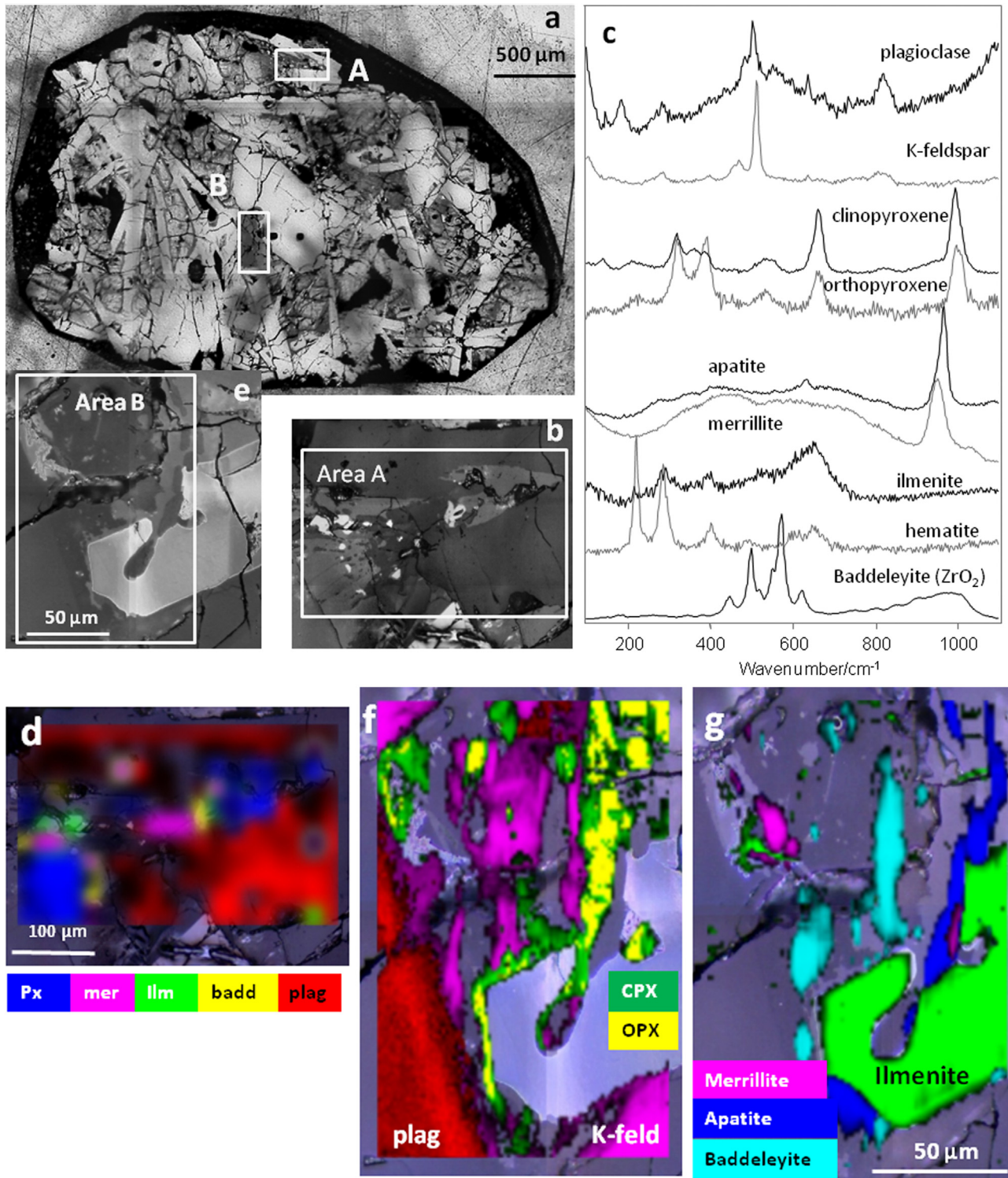


Fig. 4. Raman imaging of an Apollo rock fragment, 14161.7062.

- Transmitted light optical image of thin section 14161.7062. Two regions investigated by Raman imaging were marked by white rectangles. Black circular spots to the right of area B are ion microprobe pits.
- White-light image of mesostasis area A.
- Typical Raman spectra of phases in this sample.
- A low spatial resolution Raman image generated from a Raman imaging data cube collected using the grid imaging mode, 442 nm laser line excitation, 50x objective, and 220 spectra to cover an area of $400 \times 300 \mu\text{m}$ with $20 \mu\text{m}$ step.
- A white-light image of mesostasis area B.
- Map of two types of feldspars and two types of pyroxenes generated from a high spatial resolution Raman image cube collected using the Streamline™ imaging mode, 532 nm laser line excitation, 50x objective. A total of 10,980 spectral data points cover a $110 \times 170 \mu\text{m}$ area with $1.3 \mu\text{m}$ per step.
- Map of two types of phosphates (apatite and merrillite), baddeleyite, and ilmenite generated from the same Raman image cube.

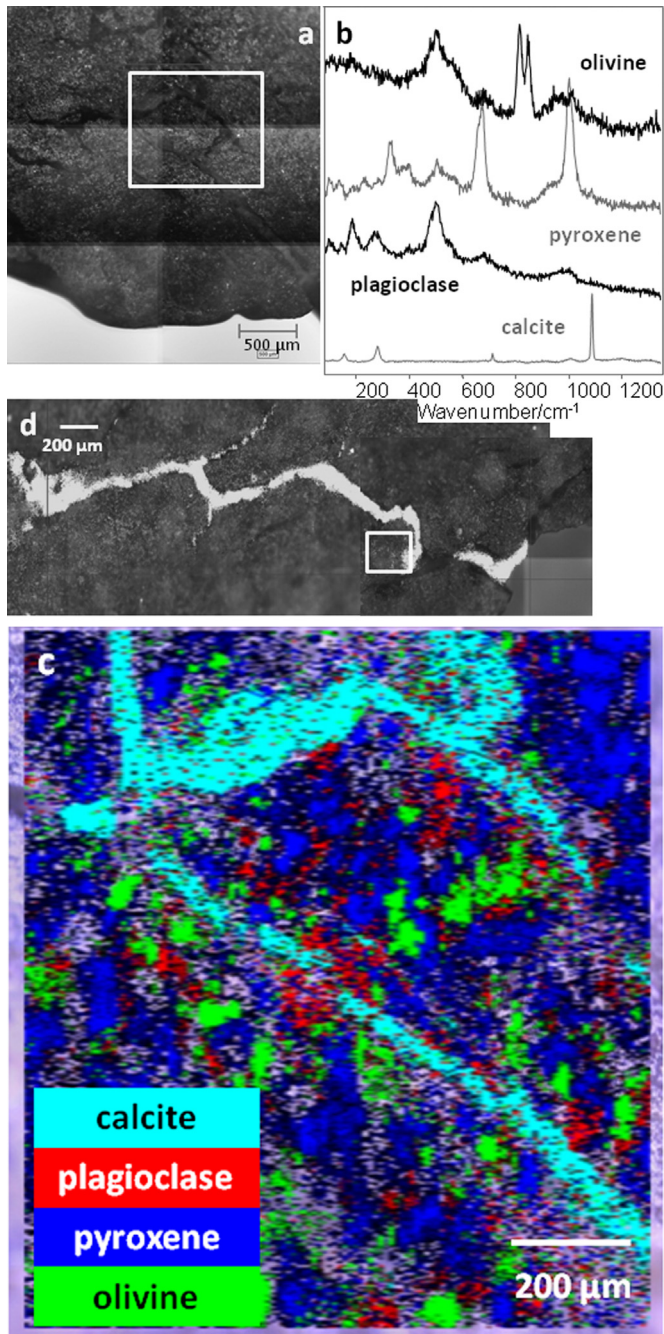


Fig. 5. Raman imaging of lunar meteorite Dhofar 1627.

- Optical image of the rock chip with a flat sawn surface. The area for Raman imaging study is marked by a white rectangle.
- Typical Raman spectra of minerals in the studied area.
- A Raman image shows the spatial distributions of four major mineral phases (based on their characteristic Raman peak positions and peak intensities) in an area marked by white rectangle in Fig. 5b. The StreamLine™ imaging mode was used with 532 nm excitation, 20x objective, $122 \times 353 = 43,066$ spectra, at $3.2 \mu\text{m}$ per step. Regardless of the uneven surface of this rock chip, the spatial correlation of these phases is clearly shown. The area without color has either weak Raman peaks or no signal.
- A combination of two Raman images taken on large areas that shows the spatial spreading of calcite (based on 1086 cm^{-1} Raman peak) in a vein system. The StreamLine™ imaging mode was used, with 532 nm excitation, 20x objective, a total of 273,356 spectra, and $3.2 \mu\text{m}$ per step.

the different reddish shades were replaced by rainbow colors to emphasize the differences in signal strength. The features (red, green, and blue colored) in Fig. 3d demonstrate that sub-micrometer spatial resolution is achieved by this measurement.

4. Raman imaging of five extraterrestrial materials

Five extraterrestrial samples of different types were selected for this preliminary Raman imaging investigation: a lunar impact-melt rock from Apollo 14 (14161,7062); a lunar meteorite found in Oman (Dhofar 1672); a martian meteorite found in Antarctica (MIL 03346); an angrite NWA 2999 found in Oman as one rare type of achondrite; and a carbonaceous chondrite, Murchison.

4.1. Raman imaging of a lunar rock chip from Apollo 14, 14161,7062

Sample 14161,7062, is a 26-mg fragment of a clast-free, KREEP-rich impact-melt rock (Fig. 4a). The bulk chemical composition and mineralogy is reported in Jolliff et al. (1991). As determined by modal petrography and electron microprobe analysis of the entire thin section, the principal mineral of the rock is plagioclase of composition An_{86-95} . Plagioclase grains are blocky to lath-like in shape, with laths up to 1 mm in length. Intergranular material is mainly pyroxene, but ilmenite and areas of fine-grained mesostasis also occur interstitially. Pyroxene grains are zoned, ranging in Mg' (mole percent $\text{Mg}/(\text{Mg} + \text{Fe})$) from 82 to 5 and in Wo content from 3–32 mol%.

We chose two mesostasis areas in this sample for Raman imaging, marked by white rectangles in Fig. 4a. In area A (Fig. 4b), we used a grid imaging mode with a point-focused laser spot ($\lambda = 442 \text{ nm}$), 50x objective, and 220 spectral points at $20 \mu\text{m}$ per step to cover a $400 \times 300 \mu\text{m}$ area. The generation of Raman images and the spatial distribution of five minerals is based on their characteristic Raman spectra, Raman peak positions (Fig. 4c), and the peak intensity over baseline. This imaging measurement was accomplished in less than 10 min. Although this Raman image has low spatial resolution (Fig. 4d), it reveals the distribution of the two major mineral grains, plagioclase and pyroxene, and the coexistence of three minor mineral grains (ilmenite, baddeleyite, and merrillite), as well as the spatial correlation of their occurrence in this mesostasis area.

In mesostasis area B (Fig. 4f), we used the StreamLine™ imaging mode with an elliptically focused laser spot ($\lambda = 532 \text{ nm}$), 50x objective, and 10,980 spectral points at $1.3 \mu\text{m}$ per step to cover a $110 \times 170 \mu\text{m}$ area. This measurement was accomplished in 2.5 h. Nine mineral phases were encountered in this mesostasis area (typical spectra shown in Fig. 4c), with two types of feldspars (plagioclase and K-feldspar), two types of pyroxenes with different $\text{Mg}/(\text{Mg} + \text{Fe} + \text{Ca})$ ratios, two phosphates (apatite and merrillite), baddeleyite (ZrO_2), ilmenite (FeTiO_3).

The StreamLine™ Raman image data cube was pre-processed in three steps, which include spectral range truncation ($120\text{--}1200 \text{ cm}^{-1}$), the removal of intensity spikes in spectra when cosmic rays hit the CCD on rare occasion during Raman imaging measurement, and a baseline correction using a 2nd order polynomial. Furthermore, in order to extract the spectral differences of three mineral pairs (e.g., two feldspars, two pyroxenes, and two phosphates) and to distinguish them in Raman imaging, spectral curve fitting was conducted on the typical Raman spectra of these pairs in order to generate a smooth Raman peak pattern for each phase. These spectral peak patterns were then used as the component spectra in a DCLS mapping procedure (WiRE 3.4, Renishaw Company) that searched through all 10,980 spectra and generated two sets of Raman images (Fig. 4f and g).

Fig. 4f shows the distribution of two feldspar and two pyroxenes, as major phases in this area. This figure demonstrates a clear spatial correlation between two pyroxene phases: the one with high $\text{Mg}/(\text{Mg} + \text{Fe} + \text{Ca})$ values occurs in the cores of mineral grains and the one with lower values occurs at the rims of grains. This spatial correlation is consistent with crystallization sequence of pyroxene from basaltic magma (impact melt in this case) and normal phase relationships. For the feldspars, plagioclase forms part of a large grain bounding the area of mesostasis, whereas K-feldspar forms in the interstitial areas bounded by coarser

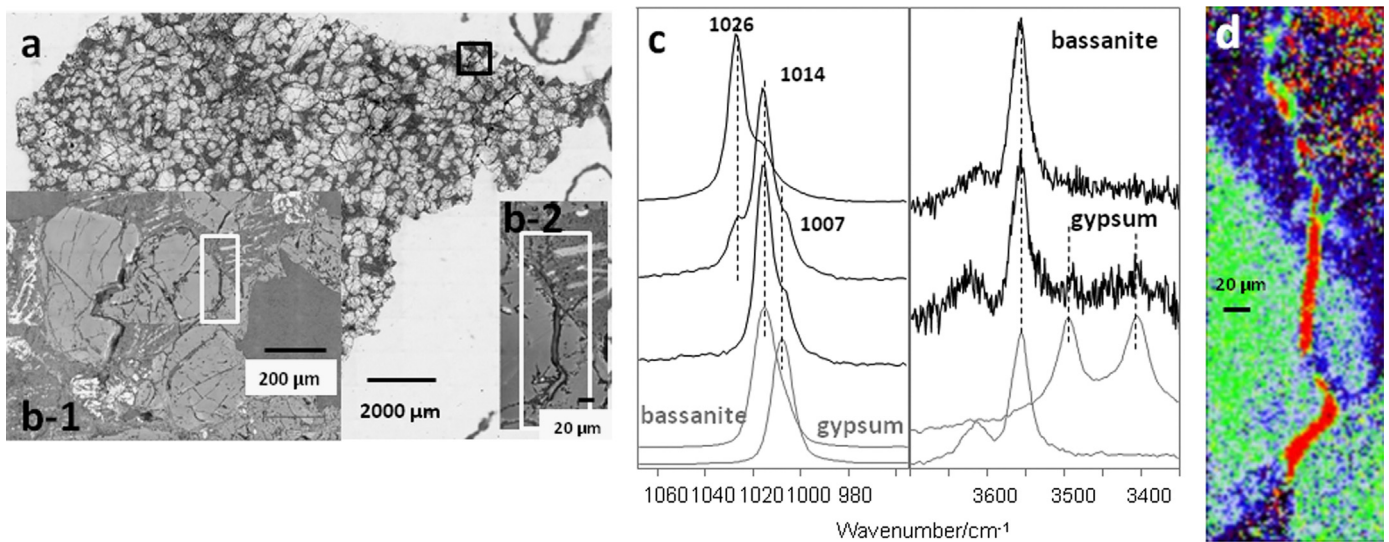


Fig. 6. Raman imaging of a martian meteorite MIL03346.

- Optical image of the thin section from a rock chip of the MIL03346 meteorite. Fractures with filling materials occur mostly in the upper portion of the rock chip. The studied area is marked by a black rectangle.
- White rectangles show where the Raman image was taken.
- Typical Raman spectra from fracture filling phases of this meteorite, in comparison with standard spectra of bassanite and gypsum. The phase with a 1026 cm^{-1} peak suggests another sulfate whose identification was interfered by epoxy peaks.
- Raman image of sulfate(s) as the filling in a vein, obtained based on Raman peaks of gypsum and bassanite. The StreamLine™ imaging mode was used, with 532 nm excitation, 50x objective, $59 \times 180 = 10,620$ spectra, and $1.3\text{ }\mu\text{m}$ per step.

plagioclase and ilmenite, consistent with the formation of K-feldspar from late-stage interstitial melt.

Fig. 4g shows the distribution of two phosphates, baddeleyite, and ilmenite. In this area, merrillite occurs as individual grains, but also coexists with apatite. The major Raman spectral peak near 967 cm^{-1} (of apatite) in the area marked by dark blue color (Fig. 4g) commonly has a shoulder on the low wavenumber side or appears as an asymmetric peak indicating mixing (overlap) with the major Raman peak of merrillite at 950 cm^{-1} (Fig. 4c). A clear grain boundary between merrillite and apatite can be seen in high resolution back-scattered electron (BSE) images, but not distinguishable in this Raman image. The spectral peaks of baddeleyite shown in Fig. 4c are actually the fluorescent emission from REE elements in this mineral, thus they do not appear in the Raman spectrum excited by the 442 nm laser line (not shown). These sharp fluorescence peaks are, however, very useful for generation of the map of this phase in mesostasis area B.

4.2. Raman imaging of a lunar meteorite, Dhofar 1627

Dhofar 1627 is an impact-melt breccia from the Moon found in Oman in 2010. Crystalline phases are approximately 75% plagioclase, 15–20% pyroxene, and 5–10% olivine, but the breccia has a glassy matrix and veins and voids contain terrestrial evaporate minerals. The studied sample chip has a flat sawn surface, but is not polished. The studied area is marked by white rectangles in Fig. 5a.

We used Streamline™ imaging mode with an elliptically focused laser spot ($\lambda = 532\text{ nm}$), 50x objective, and 43,066 spectral points at $3.2\text{ }\mu\text{m}$ per step to cover a $390 \times 1130\text{ }\mu\text{m}$ area. This measurement was accomplished in 2.5 h. Four mineral phases were encountered (typical spectra in Fig. 5b), olivine, feldspars, pyroxene, and calcite CaCO_3 . Fig. 5c clearly shows the spatial distribution of these phases, irrespective of the uneven surface of this rock chip. Fig. 5d combines two Raman images using a larger excitation laser spot ($\lambda = 532\text{ nm}$ excitation, 20x objective, StreamLine™ imaging mode, a total of 273,356 spectra, at $3.2\text{ }\mu\text{m}$

per step). The image reveals the vein system filled by calcite in this grain that starts from the grain surface and spreads through the main veinlets and fine fractures. The vein system was likely formed during the impact that launched the meteorite from the Moon. The calcite is a precipitated phase from fluids during exposure of the meteorite on the desert surface in Oman (Korotev, 2012). "Missing" calcite in a few veins could be caused by later events, such as on-site weathering, human collection activities, and sample preparation. We noticed some calcite grains also occur in the matrix of this rock (near a vein, marked by a white rectangle in Fig. 5d). The current hypothesis is that is due to smearing from calcite filling veins during the sample preparation process, likely sawing.

4.3. Raman imaging of a Martian meteorite, MIL03346

MIL03346, which belongs to the nakhlite group (orthopyroxenite) of martian meteorites, was collected from the Miller Range in Antarctica. It has been intensively studied owing to its unique properties, especially for its importance as an indicator of geologically hydrothermal alteration as part of its martian aqueous interaction history (Day et al., 2006; McCubbin et al., 2009; Changela and Bridges, 2011). MIL 03346 is among the most oxidized and least equilibrated of the nakhlites and displays the largest amount of intercumulus phases. The low-temperature vein alteration assemblage in MIL 03346 is reported to have smectite, iddingsite, jarosite, gypsum, Ca-phosphates, and residual glass (Herd, 2006; Sautter et al., 2006; Vicenzi et al., 2007; Hallis and Taylor, 2011; Stopar et al., 2013). The martian origin of the vein fillings in nakhlites has been established because the veins in Nakhla and Lafayette are seen to be truncated by the fusion crust (Gooding et al., 1991; Treiman et al., 1993). Recently, Hallis et al. (2012, 2013) conducted a deuterium/hydrogen (D/H) ratio analysis of MIL 03346 to distinguish between terrestrial and martian secondary alteration phases. Elevated δD values in alteration veins relative to terrestrial materials suggest that the veins have a martian origin.

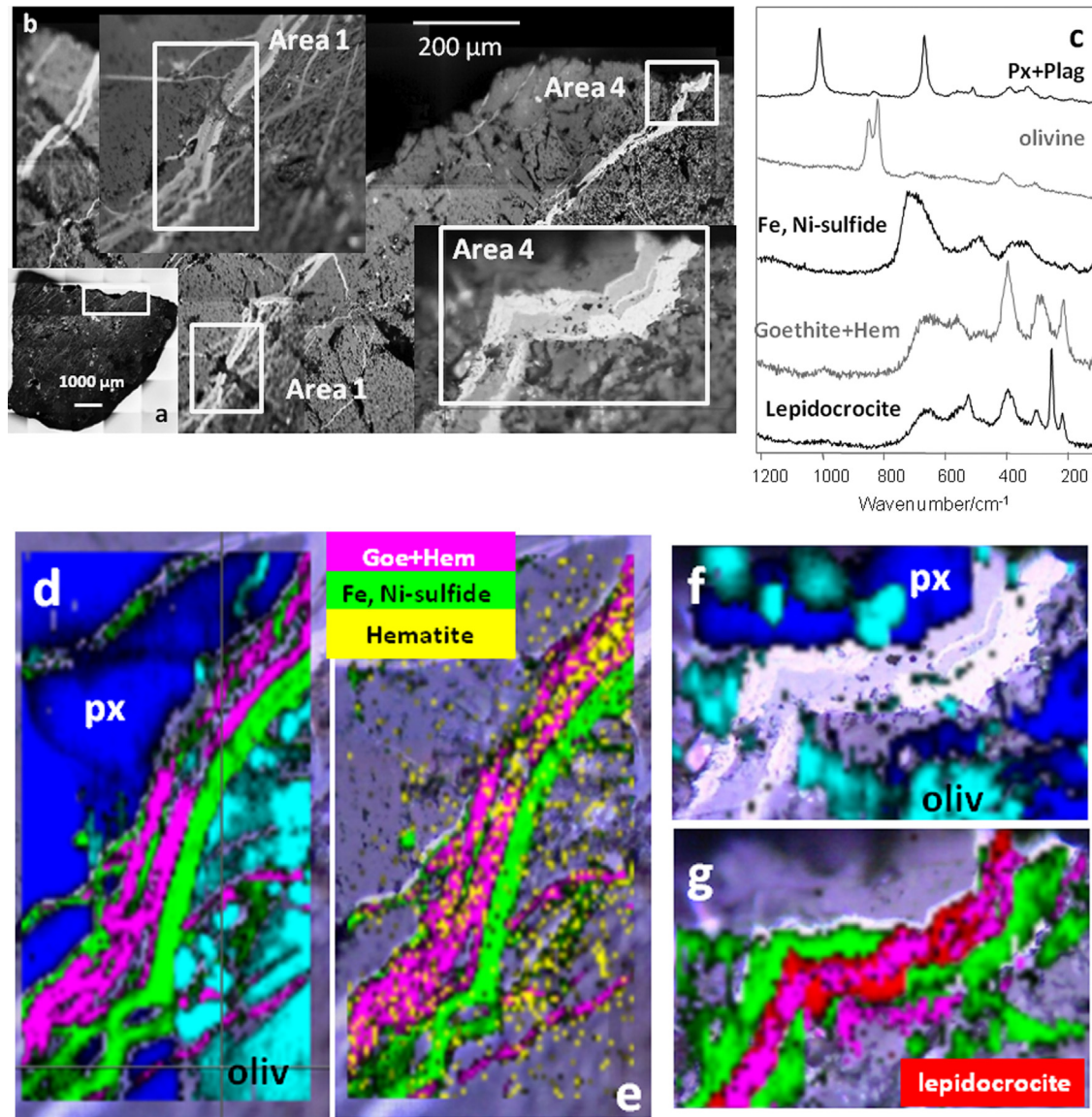


Fig. 7. Raman imaging of achondrite angrite NWA2999.

- a. Optical image of a rock chip of NWA2999. Hollows and veins with fillings spread across the entire rock chip. The studied areas are marked by a white rectangle.
 b. Areas #1 and #4 (white rectangles) on a rock chip where Raman spot analyses and a Raman image data cube were collected.
 c. Typical Raman spectra from NWA2999.
 d. Raman image of matrix and vein-filling phases in area #1.
 e. Raman image of Fe-bearing phases.
 f. Raman image of matrix minerals, olivine and pyroxene in area #4.
 g. Raman image of goethite (+hematite), lepidocrocite, and FeNi-sulfide in area #4.

A thin section, MIL03346,168, from this meteorite was used for this Raman imaging study (Fig. 6a). We note that many fractures with filling materials occur mostly in one side of the rock chip. A black rectangle in Fig. 6a shows the zones of this Raman study. White rectangles in Fig. 6b-1, b-2 mark where Raman spot-analyses and a Raman image data cube were collected.

Our study of MIL03346 concentrated on the vein-filling phases. The detailed study is still ongoing, so we present here only one Raman image to show the richness of information that can be obtained. Fig. 6c shows the typical Raman spectra of three sulfate phases that were identified in a single vein shown in Fig. 6b-2. When compared with the standard Raman spectra, we confirmed that the two major phases are bassanite $\text{CaSO}_4 \cdot \frac{1}{2}\text{H}_2\text{O}$ and gypsum $\text{CaSO}_4 \cdot 2\text{H}_2\text{O}$. The third phase has a major Raman peak (1026 cm^{-1}) that matches with γ -anhydrite (CaSO_4) (Chio et al.,

2004), alunite $\text{KAl}_3(\text{SO}_4)_3(\text{OH})_6$ (McCollom et al., 2014), and paraquimbite $\text{Fe}_2(\text{SO}_4)_3 \cdot 9\text{H}_2\text{O}$ (Wang et al., 2012). Its definitive identification, however, is impaired by the interference of Raman peaks from the epoxy used to prepare the thin section. A major challenge in collecting Raman spectra from this meteorite is that it is heavily fractured, thus epoxy is exposed at the surface of this thin section during sample mounting (epoxy impregnation) and polishing. The epoxy contributes many Raman peaks of its own and produces a high spectral background. The interference of Raman peaks from epoxy prevents definitive identification of the third sulfate in the vein.

The Raman image of vein-filling sulfates (Fig. 6d) was obtained based on the peak intensity over baseline of the gypsum Raman peak at $\sim 1008 \text{ cm}^{-1}$ and bassanite, $\sim 1015 \text{ cm}^{-1}$. The StreamLine™ imaging mode was used, with 532 nm excitation, 50x objective, $59 \times 180 = 10,620$ spectra, at $1.3 \mu\text{m}$ per step. We are investigating

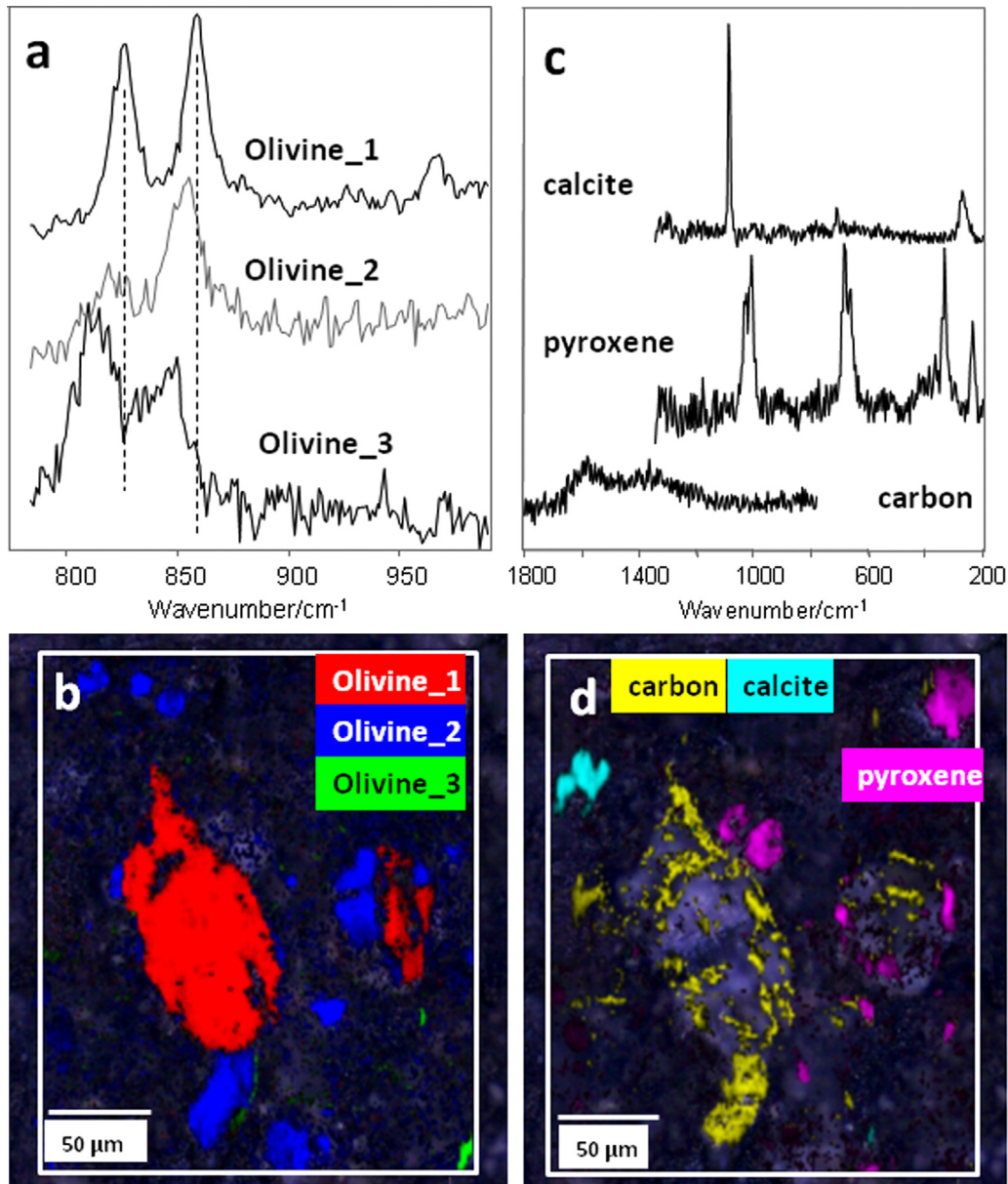


Fig. 8. Raman imaging of a rock chip from the Murchison meteorite.

a. Raman spectra of three types of olivine grains (peak shifts marked by two dotted lines) in the examined area of this Murchison sample.

b. A Raman image shows the distribution of olivine grains with different Mg/(Mg+Fe) ratios (olivine-1,-2, -3).

c. Raman spectra of carbon, calcite, and pyroxene.

d. Raman image shows the distribution of carbonaceous material, calcite, and pyroxene.

approaches to overcome the interference of epoxy Raman signals to obtain the spatial distribution of all of the sulfates from a Raman image data cube obtained from this meteorite (Ling and Wang, 2015).

4.4. Raman imaging of meteorite northwest Africa 2999

NWA2999 is an angrite meteorite found in Morocco or Algeria in 2004 (Fig. 7a). The meteorite consists mainly of olivine, pyroxene, plagioclase, and iron metal that has partially oxidized with exposure in the desert (A. J. Irving et al. in Connolly et al., 2006). Hollows and veins with fillings are spread over the entire rock chip. The studied area near the upper edge is marked by a white rectangle in Fig. 7a.

Fig. 7b shows the details of a studied area (marked as a white rectangle in Fig. 7a), in which Raman images from four regions

(Area 1, 2, 3, 4) were taken. The StreamLine™ imaging mode was used in the measurements of these areas, with 532 nm excitation, 50x objective, and 1.3 μm per step. We found that in this meteorite the vein-filling phases have the most variations in molecular forms. The major mineral phases in the matrix are olivine, pyroxene, and plagioclase (typical Raman spectra in Fig. 7c). Fractures pass along boundaries between mineral grains (Fig. 7d) and through mineral grains (Fig. 7f). With reflected-light optical microscopy, the vein-filling materials show two types of reflectance (Fig. 7f). The bright phase near the vein-wall has a Raman spectral pattern that matches best with FeNi-sulfides (typical spectra in Fig. 7c). The less reflective phase, occurs in some cases in the center of veins and consists of a mixture of goethite, FeOOH, and hematite, Fe₂O₃. In three of four areas where Raman images were taken, abundant tiny hematite grains spread over the matrix and vein area (Fig. 7e). We also found a new crystalline FeOOH

phase, lepidocrocite, coexisting with the mixture of goethite and hematite in the center of a large vein of Area 4 (Fig. 7g, i.e., there are three chemical and structural distinct phases filling the vein), which is near the edge of this meteorite grain. The occurrence and the spatial distribution of these Fe-rich species reflect the chemistry of vein-filling fluids; and the changes of environmental conditions during the formations of these species.

4.5. Raman imaging of a carbonaceous meteorite, Murchison

The Murchison meteorite is a CM2 carbonaceous chondrite, one that experienced extensive alteration by water-rich fluids on its parent body before falling to Earth. It is rich in carbon and contains over 15 amino acids. The studied sample has a fine-grained black matrix with embedded light-toned chondrules in which the major phases are olivine and pyroxene.

The StreamLine™ imaging mode was used to obtain a Raman image from a small area of a flat-sawn piece of the meteorite. The image cube was taken with 532 nm excitation, 50x long working distance objective, $170 \times 172 = 29,240$ spectra, and 1.3 μm per step.

The major mineral phase in the meteorite, olivine $[(\text{Fe},\text{Mg})_2\text{SiO}_4]$ shows a wide variation in $\text{Mg}/(\text{Mg}+\text{Fe})$ ratio. Fig. 8a shows three Raman spectra of olivine grains in the meteorite with an obvious position shift of the olivine doublet peak which represents approximate $\text{Mg}/(\text{Mg}+\text{Fe})$ ratios of 1.0, 0.8, 0.3 (type-I, -II, -III) respectively. When using the positions of these olivine doublets to build a Raman image, we obtained the spatial distribution of three types of olivine in the studied area (Fig. 8b). The central grain is Mg-rich type-I olivine ($> 100 \mu\text{m}$, colored in red). The type-II olivine has much smaller grain size (30–40 μm , colored in blue). The Fe-rich (type-III) olivine appears only as a tiny grain ($< 10 \mu\text{m}$, colored in green) at the corner of the imaged area. This image provides qualitative information on the modal proportions of three olivine types.

We obtained spectra for 2–4 calcite grains in the meteorite (spectrum shown in Fig. 8c). These calcite grains have grain size $< 10 \mu\text{m}$ and are clustered together (Fig. 8d, colored in light-blue). Fig. 8d also shows the occurrence of carbonaceous material (colored in yellow) with very low crystallinity (shown as broad Raman peaks in Fig. 8c) that envelope the type-I and type-II olivine grains. The occurrence of pyroxene grains (colored in purple) apparently corresponds with type-II olivine.

The spatial distribution of these mineral species in this carbonaceous chondrite indicate the aggregation of major silicate phases with a large range of chemistry formed at different temperatures and in different parts of the solar nebula. Mixing with carbonaceous materials occurred during this accretion, shown as the envelopment of C-materials on olivine and pyroxene grains (Fig. 8d).

5. Summary

The results from Raman imaging studies of three terrestrial samples and five extraterrestrial samples demonstrate the capability of this technique to extract molecular species information with spatial correlations. From these data, one can infer the processes that produced or affected these species. This study shows the strength of Raman imaging for the investigation of precious samples returned by planetary missions. It also demonstrated that even by using a simplified Raman imaging technology, e.g., grid scan (Fig. 4d, Haskin et al., 1997; Wang and Lambert, 2013) or on a roughly prepared surface of planetary materials (Fig. 5c, e.g., using a Rock Abrasion Tool during Mars Exploration Rovers mission), extremely useful information on the properties of molecular species and their genetic relationship can be extracted

from a short duration of measurement. These information will add significant value to the science return of a planetary mission.

Acknowledgments

The purchase of the inVia Raman imaging system was jointly funded by NASA's Major Planetary Equipment Program under Mars Fundamental Research project NNX10AM89G, and by the McDonnell Center for the Space Sciences, Department of Earth and Planetary Sciences, and School of Arts and Sciences at Washington University in St. Louis. We also appreciate support from NASA for an ASTEP project NNX09AE80A subcontract #08-SC-1072 and for an MoO project (RLS-ExoMars) contract #1295053, both of which are related to Planetary Raman Spectroscopy. We are grateful to the following individuals for kindly providing samples for this study: Prof. Robert F. Dymek of Washington University in St. Louis for OGG-145, and Prof. Maud M. Walsh of Louisiana State University for the SA chert.

References

- Changela, H.G., Bridges, J.C., 2011. Alteration assemblages in the nakhlites: variation with depth on Mars. *Meteorit. Planet. Sci.* 45, 1847–1867.
- Chio, C.H., Sharma, S.K., Muenow, D.W., 2004. Micro-Raman studies of gypsum in the temperature range between 9 K and 373 K. *Am. Miner.* 89, 390–395.
- Connolly Jr., H.C., Zipfel, J., Grossman, J.N., Folco, L., Smith, C., Jones, R.H., Righter, K., Zolensky, M., Russell, S.S., Yamaguchi, A., Benedix, G.K., Cohen, B.A., 2006. The Meteoritical Bulletin (No. 90, 2006 September). *Meteorit. Planet. Sci.* 41, 1383–1418.
- Day, J.M.D., Taylor, L.A., Floss, C., McSween Jr., H.Y., 2006. Petrology and chemistry of MIL 03346 and its significance in understanding the petrogenesis of nakhlites on Mars. *Meteorit. Planet. Sci.* 41, 581–606.
- Dymek, R.F., Owens, B.E., 2001. Chemical assembly of Archaean anorthosites from amphibolite- and granulite-facies terranes, West Greenland. *Contrib. Mineral. Petr.* 141, 513–528.
- Edwards, H.G.M., Moody, C.D., Villar, S.E.J., Wynn-Williams, D.D., 2005a. Raman spectroscopic detection of key biomarkers of cyanobacteria and lichen symbiosis in extreme Antarctic habitats: evaluation for Mars lander missions. *Icarus* 174, 560–571.
- Edwards, H.G.M., Villar, S.E.J., Parnell, J., Cockell, C.S., Lee, P., 2005b. Raman spectroscopic analysis of cyanobacterial gypsum halotrophs and relevance for sulfate deposits on Mars. *Analyst* 130, 917–923.
- Edwards, H.G.M., Villar, S.E.J., Pullan, D., Hofmann, B.A., Hargreaves, M.D., Westall, F., 2007. Morphological biosignatures from relict fossilised sedimentary geological specimens: a Raman spectroscopic study. *J. Raman. Spectrosc.* 38, 1352–1361.
- Freeman, J.J., Wang, Alian, Kuebler, K.E., Haskin, L.A., 2008. Characterization of Natural Feldspar by Raman Spectroscopy for Future Planetary Exploration. *Can. Mineral* 46 (6), 1477–1500.
- Fries, M., Steele, A., 2008. Graphite whiskers in CV3 Meteorites. *Science* 320, 91–93.
- Gooding, J.L., Wentworth, S.J., Zolensky, M.E., 1991. Aqueous alteration of the Nakhla meteorite. *Meteoritics* 26, 135–143.
- Gogots, V., Baek, C., Kirscht, F., 1999. Raman microspectroscopy study of processing-induced phase transformations and residual stress in silicon. *Semicond. Sci. Tech* 14, 936–944.
- Hallis, L.J., Taylor, G.J., 2011. Comparisons of the four Miller Range nakhlites, MIL 03346, 090030, 090032 and 090136: textural and compositional observations of primary and secondary mineral assemblages. *Meteorit. Planet. Sci.* 46, 1787–1803.
- Hallis, L.J., Taylor, G.J., Nagashima, K., Huss, G.R., Needham, A.W., Franchi, I.A., Grady, M.M., 2012. Hydrogen isotope analyses of alteration phases in the nakhlite martian meteorites. *Geochim. Cosmochim. Acta.* 97, 105–119.
- Hallis, L.J., 2013. Alteration assemblages in the Miller Range and Elephant Moraine regions of Antarctica: Comparisons between terrestrial igneous rocks and martian meteorites. *Meteorit. Planet. Sci.* 48, 165–179.
- Haskin, L.A., Wang, Alian, Rockow, K.M., Jolliff, B.L., Korotev, R.L., Viskupic, K.M., 1997. Raman spectroscopy for mineral identification and quantification for in-situ planetary surface analysis: a point count method. *J. Geophys. Res.* 102, 19293–19306.
- Herd, C.D.K., 2006. An occurrence of jarosite in Mil 03346: implications for conditions of martian aqueous alteration. *Meteorit. Planet. Sci.* 41, A74.
- Jolliff, B.L., Korotev, R.L., Haskin, L.A., 1991. Geochemistry of 2–4 mm particle from Apollo 14 soil(14161) and implication regarding igneous component and soil-forming processes. *Proc. Lunar Planet. Sci.* 21, 193–219.
- Korotev, R.L., 2012. Lunar meteorites from Oman. *Meteorit. Planet. Sci.* 47, 1365–1402. <http://dx.doi.org/10.1111/j.1945-5100.2012.01393.x>.
- Ling, Zongcheng, Wang, Alian, 2015. Spatial distributions of secondary minerals in the Martian meteorite MIL 03346,168 determined by Raman spectroscopic imaging. *J. Geophys. Res.*, in revision.

- Marshall, C.P., Leuko, S., Coyle, C.M., Walter, M.R., Burns, B.P., Neilan, B.A., 2007. Carotenoid analysis of halophilic archaea by resonance Raman spectroscopy. *Astrobiology* 7, 631–643. <http://dx.doi.org/10.1089/ast.2006.0097>.
- Marshall, C.P., Wang, Alian, 2010. Considerations for the collection of Raman spectra of potential Martian biosignatures, Abstract for the 9th International Conference on Raman spectroscopy Applied to the Earth Sciences, Sydney, Australia.
- Marshall, C.P., Edwards, H.G.M., Jehlicka, J., 2010. Understanding the Application of Raman Spectroscopy to the Detection of Traces of Life. *Astrobiology*, 10. <http://dx.doi.org/10.1089/ast.2009.0344>.
- McCullom, T.M., Ehlmann, B.L., Wang, Alian, Hynke, B.M., Moskowitz, B., Berquó, T.S., 2014. Detection of Iron Substitution in Natroalunite and Potential Implications for Mars, accepted by *Am. Minerals*.
- McCubbin, F.M., Tosca, N.J., Smirnov, A., Nekvasil, H., Steele, A., Fries, M., Lindsley, D. H., 2009. Hydrothermal jarosite and hematite in a pyroxene-hosted melt inclusion in martian meteorite Miller Range (MIL) 03346: implications for magmatic-hydrothermal fluids on Mars. *Geochim. Cosmochim. Acta* 73, 4907–4917.
- Nasdala, L., Beyssac, O., Schopf, J.W., Bleisteiner, B., 2012. Application of Raman-based images in the Earth sciences. In: Zoubir, A. (Ed.), *Raman Imaging – Techniques and Applications*. Springer Series in Optical Sciences, vol. 168. Springer, Berlin, Heidelberg, pp. 145–187.
- Nemanich, R.J., Solin, S.A., 1979. First- and second-order Raman scattering from finite-size crystals of graphite. *Phys. Rev. B* 20, 392–401.
- Pasteris, J., Wopenka, B., 1991. Raman spectra of graphite as indicators of degree of metamorphism. *Can. Mineral* 29, 1–9.
- Pavlov, A.A., Vasilyev, G., Ostryakov, V.M., Pavlov, A.K., Mahaffy, P., 2012. Degradation of the organic molecules in the shallow subsurface of Mars due to irradiation by cosmic rays. *Geophys. Res. Lett.* 39, L13202. <http://dx.doi.org/10.1029/2012GL052166>.
- Rull, Fernando, Martínez-Frías, J., 2006. Raman spectroscopy goes to Mars. *Spectrosc. Eur.* 18 (1).
- Sautter, V., Jambon, A., Boudouma, O., 2006. Cl-amphibole in the nakhlite Mil 03346: evidence for sediment contamination in a martian meteorite. *Earth. Planet. Sci. Lett.* 252, 45–55.
- Seddio, SM, Korotev, RL, Jolliff, BL, and Wang A (2015) Silica polymorphs in lunar granite: implications for granite petrogenesis on the Moon. *Am. Mineral.* in press. <http://dx.doi.org/10.2138/am-2014-5058>.
- Steele, A., Fries, M.D., Amundsen, H.E.F., Mysen, B.O., Fogel, M.L., Schweizer, M., Boctor, N.Z., 2007. Comprehensive imaging and Raman spectroscopy of carbonate globules from Martian meteorite ALH84001 and a terrestrial analogue from Svalbard. *Meteorite Planet. Sci.* 42, 1549–1566.
- Steele, A., McCubbin, F.M., Fries, M., Glamoclija, M., Kater, L., Nekvasil, H., 2010. Graphite in an Apollo 17 impact melt breccia. *Science* 329, 51.
- Steele, A., McCubbin, F.M., Fries, M.D.F., Golden, D.C., Ming, D.W., Benning, L.G., 2012a. Graphite in the Martian Meteorite ALH 84001. *Am. Mineral.* 97, 1256–1259.
- Steele, A., McCubbin, F.M., Fries, M., Kater, L., Boctor, N.Z., Fogel, M.L., Conrad, P.G., Glamoclija, M., Spencer, M., Morrow, A.L., Hammond, M.R., Zare, R.N., Vicenzi, E.P., Siljeström, S., Bowden, R., Herd, C.D.K., Mysen, B.O., Shirey, S.B., Amundsen, H.E.F., Treiman, A.J.T., Bullock, E.S., Ju, A.J.T., 2012b. A reduced organic carbon component in Martian Basalts. *Science* 337, 212–215.
- Stopar, J.D., Taylor, G.J., Norman, M.D., Hallis, L.J., Velbel, M.A., Vicenzi, E.P., 2013. Element abundances, patterns, and mobility in nakhlite Miller Range 03346: Implications for aqueous alteration. *Geochim. Cosmochim. Acta* 112, 208–225.
- Treiman, A.H., Barrett, R.A., Gooding, J.L., 1993. Preterrestrial aqueous alteration of the Lafayette (SNC) meteorite. *Meteoritics* 28, 86–97.
- Vicenzi, E.P., Fries, M., Fahey, A., Rost, D., Greenwood, J.P., Steele, A., 2007. Detailed elemental, mineralogical, and isotopic examination of jarosite in martian meteorite MIL 03346. *Lunar Planet. Sci. Conf.* 2335 (XXXVIII. #).
- Villar, S.E.J., Edwards, H.G.M., Worland, M.R., 2005. Comparative evaluation of Raman spectroscopy at different wavelengths for extremophile exemplars. *Orig. Life Evol. Biosph.* 35, 489–506.
- Villar, S.E.J., Edwards, H.G.M., 2006. Raman spectroscopy in astrobiology. *Anal. Bioanal. Chem.* 384, 100–113.
- Wang, Alian, Dhamelincourt, P., Dubessy, J., Guerard, D., Landais, P., Lelaurain, M., 1989. Characterization of graphite alteration in an uranium deposit by micro Raman spectroscopy, X ray diffraction, transmission electron microscopy and scanning electron microscopy. *Carbon* 27, 209–218.
- Wang, Alian, Jolliff, B.L., Haskin, L.A., 1995. Raman spectroscopy as a method for mineral identification on lunar robotic exploration missions. *J. Geophys. Res.* 100, 21189–21199.
- Wang, Alian, Haskin, A.L., Cortez, E., 1998. A Raman spectroscopic sensor for in situ mineral characterization on planetary surface. *Appl. Spectrosc.* 52, 477–487.
- Wang, Alian, Haskin, L.A., Kuebler, K.E., Jolliff, B.L., Walsh, M.M., 2001. Raman Spectroscopic Detection of Graphitic Carbon of Biogenic Parentage in an Ancient South African Chert, Abstract #1423, 32nd LPSC.
- Wang, Alian, Haskin, L.A., Lane, A.L., Wdowiak, T.J., Squyres, S.W., Wilson, R.J., Hovland, L.E., Manatt, K.S., Raouf, N., Smith, C.D., 2003. Development of the Mars Microbeam Raman Spectrometer (MMRS). *J. Geophys. Res.* 108 (E1), 5005. <http://dx.doi.org/10.1029/2002JE001902>.
- Wang, Alian, Ling, Z.C., Freeman, J.J., 2012. Stability field and Phase Transition Pathways of Hydrous Ferric Sulfates in the Temperature Range 50 °C to 5 °C: Implication for Martian Sulfates. *Icarus* 218, 622–643. <http://dx.doi.org/10.1016/j.icarus.2012.01.003>.
- Wang, Alian, Lambert, J.L., 2013. Compact Integrated Raman Spectrometer (CIRS) for In Situ Phase Characterization of during Robotic Exploration Missions on the Surface of Planetary Bodies, Abstract #220 for Low Cost Planetary Mission Conference, CalTech.
- Walsh, M.M., 1992. Microfossils and possible microfossils from the early Archean Onverwacht group, Barberton mountain land, South Africa. *Precambrian Res.* 54, 271–293.
- Walsh, M.M., Lowe, D.R., 1985. Filamentous microfossils from the 3,500-Myr old Onverwacht Group, Barberton Mountain Land, South Africa. *Nature* 314, 530–532.
- Wopenka, B., Pasteris, J., 1993. Structural characterization of kerogens to granulite-facies graphite: Applicability of Raman microprobe spectroscopy. *Am. Mineral.* 78, 533–557.